Catalysis Today 158 (2010) 35–43

Contents lists available at ScienceDirect

Catalysis Today

journal homepage: www.elsevier.com/locate/cattod

Synthesis of CeO_2, ZrO_2, $Ce_{0.5}Zr_{0.5}O_2$, and TiO_2 nanoparticles by a novel oil-in-water microemulsion reaction method and their use as catalyst support for CO oxidation

Margarita Sanchez-Dominguez[a], Leonarda F. Liotta[b], Gabriella Di Carlo[d], Giuseppe Pantaleo[b], Anna M. Venezia[b], Conxita Solans[a], Magali Boutonnet[c,*]

[a] Institute of Advanced Chemistry of Catalonia (IQAC), Spanish Council for Scientific Research (CSIC), CIBER BBN, Jordi Girona 18-26, 08034 Barcelona, Spain
[b] Institute of Nanostructured Materials, ISMN-CNR, Via Ugo la Malfa 153, 90146 Palermo, Italy
[c] Royal Institute of Technology (KTH), Department of Chemical Engineering and Technology, Div. of Chemical Technology, Teknikringen 42, S-10044 Stockholm, Sweden
[d] ISMN-CNR, Via Salaria km 29300, 00015 Monterotondo Stazione, Rome, Italy

ARTICLE INFO

Article history:
Available online 2 July 2010

Keywords:
Oil-in-water microemulsion
Metal oxide
Gold
Catalysts
Titania
Ceria
Ceria/zirconia
Zirconia
CO oxidation

ABSTRACT

A novel and straightforward approach for the synthesis of mesoporous inorganic oxide nanoparticles, with a small particle size and high specific surface area is reported, by using oil-in-water microemulsions, in contrast to the typically used water-in-oil microemulsion method. The new strategy implies the use of organometallic precursors, dissolved in nanometer-scale oil droplets (stabilised by surfactant), and dispersed in a continuous aqueous phase. The potential of this approach is explored for producing nanocrystalline ceria, zirconia, ceria/zirconia mixed oxide and titania. Nanocrystalline cubic CeO_2 and $Ce_{0.5}Zr_{0.5}O_2$ were obtained under soft conditions, whilst ZrO_2 and TiO_2 presented wide X-ray diffraction peaks. The specific surface area (SSA) of the obtained materials was in the order of 200–370 m^2/g and the particle size was very small (~2–3 nm). The materials were calcined at 400 °C after which a high SSA was maintained (100–150 m^2/g) and the crystallinity was improved, yielding tetragonal phases for both TiO_2 (anatase) and ZrO_2. The potential of the calcined materials as catalyst support was explored in the CO oxidation reaction by doping the oxides with Au (2 wt%). The obtained results demonstrate the feasibility of this approach for the preparation of various supports with high SSA for catalytic purposes.

1. Introduction

A key requirement for all catalysts in any application is a high active surface area or high metal dispersion. One type of synthesis media for catalysts preparation offering such high surface area is microemulsions. These systems are transparent and thermodynamically stable colloidal dispersions in which two liquids initially immiscible (typically water and oil) coexist in one phase due to the presence of a monolayer of surfactant molecules. [1] Depending on the ratio of oil and water and on the hydrophilic–lipophilic balance (HLB) of the surfactant, microemulsions can exist as oil-swollen micelles dispersed in water (oil-in-water microemulsions), or water-swollen inverse micelles dispersed in oil (water-in-oil microemulsions). The characteristic size of microemulsion droplets is very small (typically below 10 nm). The preparation of nanoparticles using microemulsion systems, due to its advantage of allowing high control of particle size, composition and structure, has been widely studied, in particular in the preparation of materials for catalytic, magnetic or ceramic uses as well as in polymer manufacture [2–4]. The first application of water-in-oil (w/o) microemulsion for the synthesis of catalytic nanoparticles was introduced in 1982 and concerns nanoparticles of noble metals [5]. Since then, this method has found a wide range of applications in the field of catalysis from room temperature reactions such as butene isomerisation to high temperature reactions such as catalytic combustion of methane [6].

Recently, we developed a novel and straightforward approach for the synthesis of inorganic nanoparticles by using oil-in-water (o/w) microemulsions [7], in contrast to the typically used water-in-oil microemulsion method. The new strategy implies the use of organometallic precursors, dissolved within oil droplets in the nanometer scale (stabilized by surfactant), and dispersed in a continuous aqueous phase. In our preliminary work, the o/w microemulsion approach was explored as proof of concept for the synthesis of metallic and metal oxide nanoparticles. The studies revealed that metallic nanoparticles (Pt, Pd, Rh) with small diame-

* Corresponding author. Tel.: +46 87908245.
E-mail address: magali@ket.kth.se (M. Boutonnet).

0920-5861/$ – see front matter © 2010 Elsevier B.V. All rights reserved.
doi:10.1016/j.cattod.2010.05.026

ter (3–6 nm) and narrow size distribution, as well as nanocrystalline metal oxide (cubic ceria) could be obtained in mild conditions. In the present study, the potential of the approach for producing nanocrystalline ceria and other related oxides (zirconia, titania, and mixed ceria/zirconia) for catalytic purposes is further explored. The different materials have been synthesized using similar microemulsion composition and reaction conditions for the sake of comparison.

The potential of the obtained nanomaterials as catalyst support is explored in the gold-catalysed CO oxidation reaction. According to the literature [8], one of the factors which influence the activity of materials for the above mentioned reaction is the size of the supported gold nanoparticles, which is determined by the method of preparation. Concerning the gold deposition procedure, there is no general rule since the optimal conditions are strongly associated with the nature of the support. In the present work, Au deposition was carried out using urea as precipitating agent in order to minimize Au loss during the synthesis [9,10]. The same procedure was used in the synthesis of all the catalysts for comparison.

The obtained results demonstrate the feasibility of the proposed synthetic procedure for the preparation of varied oxide nanocrystalline materials with high SSA and small crystallite size for catalytic applications.

2. Experimental section

2.1. Materials

Synperonic® 10/6 was a gift from Croda. Cerium (III) 2-ethylhexanoate (*Ce-EH*) was purchased from Aldrich; zirconium (IV) 2-ethylhexanoate (Zr-EH) and titanium (IV) 2-ethylhexanoate (Ti-EH) were from Alfa Aesar. Hexane (Suprasolv, for gas chromatography) and ammonia 25% were purchased from Merck. Isopropanol was purchased from Carlo Erba.

2.2. Preparation of oxide nanoparticles by the o/w microemulsion reaction method

The microemulsion system studied was: water/Synperonic® 10/6/hexane. The procedure for the synthesis of the different oxides was as follows. The microemulsion containing the corresponding organometallic precursor was prepared by mixing appropriate amounts of surfactant, oil component (as a solution of the corresponding organometallic precursor (s)) and deionized water. This composition was: 64.5% water, 21.5% surfactant and 14% oil phase for TiO_2, ZrO_2 and $Ce_{0.5}Zr_{0.5}O_2$, and 60% water, 20% surfactant and 20% oil phase for CeO_2. The mixture was stirred by magnetic stirring at 25 °C (for TiO_2) or 35 °C (for CeO_2, ZrO_2 and $Ce_{0.5}Zr_{0.5}O_2$) until a homogeneous, transparent, and fluid isotropic phase was obtained. The microemulsion was kept at 25 °C or 35 °C. Next, NH_3 25 wt% was added under vigorous stirring, up to pH 10–11; a turbid yellowish colour appeared eventually indicating the formation of CeO_2 and $Ce_{0.5}Zr_{0.5}O_2$ nanoparticles, whilst it was turbid white for ZrO_2 and TiO_2 nanoparticles. The reaction mixture was kept stirring overnight, followed by centrifugation and washing cycles (ethanol and chloroform) and dried at 70 °C. Calcination was carried out by a heating rate of 5 °C/min and keeping at 400 °C during 2 h in an air atmosphere.

2.3. Characterization of the oxide nanomaterials

Particle size and morphology were investigated by High Resolution Transmission Electron Microscopy (HRTEM). A drop of reaction mixture (dispersion of nanoparticles in microemulsion media) was sonicated in isopropanol (2 ml), and a drop of this dispersion was deposited onto a formvar/carbon copper grid. Observation was carried out using a HRTEM 300KV Philips CM30 (Super-Twin objective polar piece, 2.0 Å resolution). Average particle size was determined from HRTEM by measuring at least 250 nanoparticles per sample (Digital Micrograph 3.4, Gatan Inc.). Dried oxide powders were characterized by X-ray diffraction (XRD). For this purpose, a Siemens Diffractometer D5000 was employed. Specific surface area (BET), pore size and pore volume were determined by nitrogen sorptiometry using a Micromeritics model Tristar 3000. For this purpose, samples were pre-outgassed at 110 °C under vacuum for 4 h prior to measurement.

2.4. Gold catalyst preparation

Au (2 wt%) catalysts were prepared over the above synthesized supports calcined at 400 °C. The deposition–precipitation method with urea, using a molar ratio urea/Au equal to 300, was used. In a typical preparation, the support (CeO_2, ZrO_2, $Ce_{0.5}Zr_{0.5}O_2$ or TiO_2) was suspended in an aqueous solution of urea and an appropriate amount of $HAuCl_4$ was added under stirring to yield a final gold concentration of 5×10^{-4} M. The suspension was heated up to 80 °C and kept refluxing under stirring for 16 h. Urea decomposition leads to a gradual rise in pH up to 7.5–8 for all the catalysts. The sample was then cooled down to room temperature, filtered and washed with ammonia solution (pH 8–9) until no chloride ions were detected by the $AgNO_3$ test. The catalysts were dried in air at 120 °C overnight.

2.5. Catalysts characterization

2.5.1. High Resolution Transmission Electron Microscopy with EDX (HRTEM/EDX)

Particle size, morphology and qualitative elemental analysis of the catalysts were investigated by HRTEM/EDX. A small amount of catalyst powder (0.2 mg) was sonicated in isopropanol (2 ml), and a drop of this dispersion was deposited onto a holey formvar/carbon copper grid. Observation and analysis was carried out using a HRTEM 200KV JEOL 2100 LAB6 (objective polar piece with a resolution of 2.3 Å), provided with an Oxford Instruments Inca Energy Dispersive X-ray (EDX) spectrometer for microanalysis (ultrathin window; resolution for the FWHM (full width at half maximum) of Mn Kα equal to 133 eV).

2.5.2. X-ray diffraction (XRD)

The as-prepared Au catalysts were characterized by X-ray diffraction (XRD), as above described. XRD analyses were also performed on the used catalysts after CO oxidation tests.

2.5.3. X-ray photoelectron spectroscopy (XPS)

The X-ray photoelectron spectroscopy analyses were performed with a VG Microtech ESCA 3000 Multilab, equipped with a dual Mg/Al anode. The spectra were excited by the unmonochromatised Al Kα source (1486.6 eV) run at 14 kV and 15 mA. The analyser operated in the constant analyser energy (CAE) mode. For the individual peak energy regions, a pass energy of 20 eV set across the hemispheres was used. Survey spectra were measured at 50 eV pass energy. The sample powders were analysed as pellets, mounted on a double-sided adhesive tape. The pressure in the analysis chamber was in the range of 10^{-8} Torr during data collection. The constant charging of the samples was removed by referencing all the energies to the C 1s set at 285.1 eV, arising from the adventitious carbon. The invariance of the peak shapes and widths at the beginning and at the end of the analyses ensured absence of differential charging. Analyses of the peaks were performed with the software provided by VG, based on non-linear least squares

fitting program using a weighted sum of Lorentzian and Gaussian component curves after background subtraction according to Shirley and Sherwood [11,12]. Atomic concentrations were calculated from peak intensity using the sensitivity factors provided with the software. The binding energy values are quoted with a precision of ±0.15 eV and the atomic percentage with a precision of ±10%.

2.6. Catalytic test procedure for CO oxidation

Catalytic tests were performed using a U shaped quartz reactor with an inner diameter of 12 mm, electrically heated in a furnace. The catalyst powder was placed on a porous quartz disk and reaction temperature was measured by a K-type thermocouple in contact with the catalytic bed. Prior to the catalytic test, the

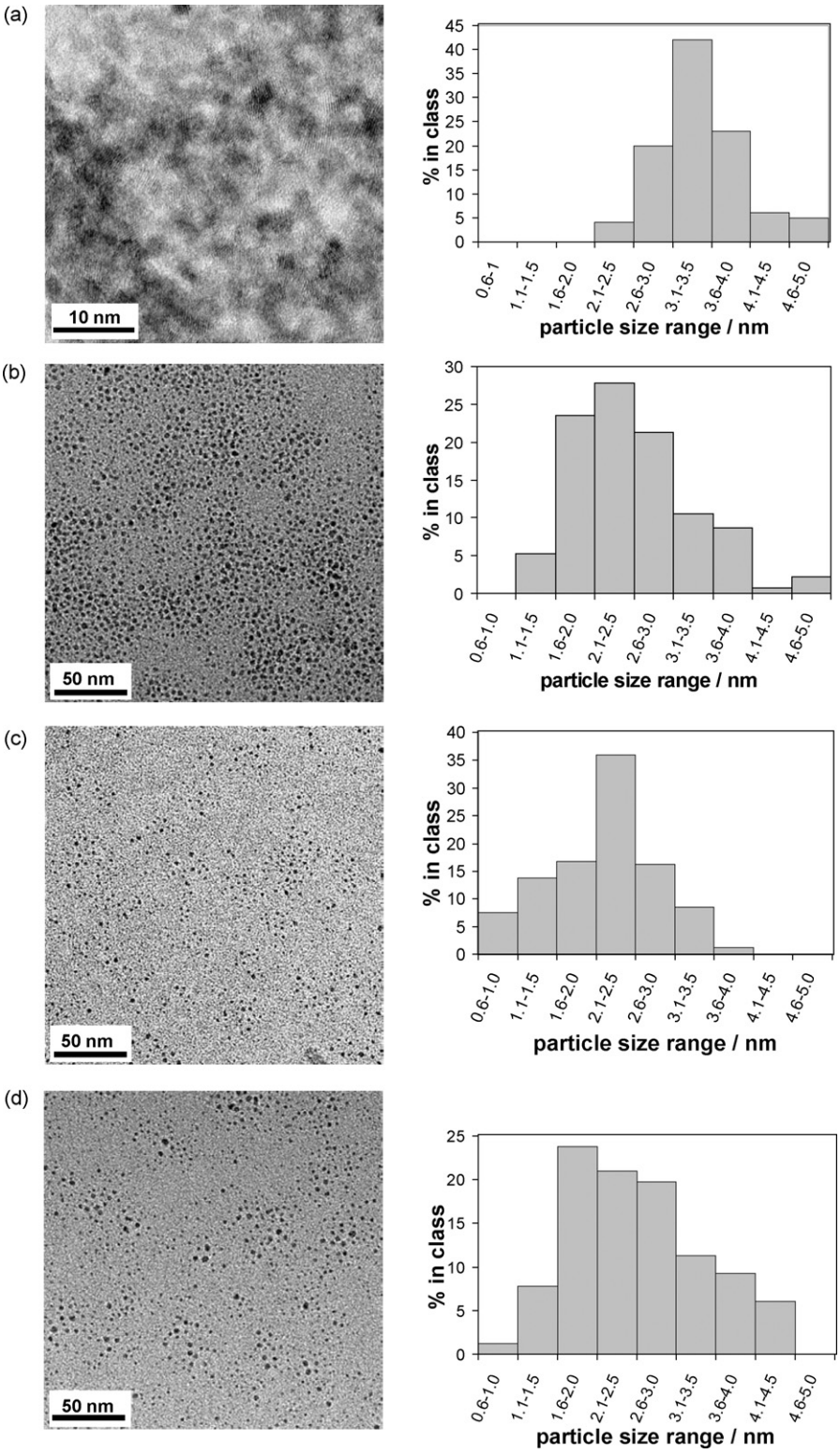

Fig. 1. HRTEM micrographs and related particle size histograms of oxide nanoparticles obtained in o/w microemulsions: (a) CeO_2; (b) $Ce_{0.5}Zr_{0.5}O_2$; (c) ZrO_2; (d) TiO_2.

catalysts (50 mg) were treated "in situ" under flowing O_2 (5 vol.% in He, 50 ml/min) at 150 °C for 1/2 h, then He was flowed during cooling to room temperature. During the tests, a gas mixture consisting of 1% of CO + 1% of O_2 in He was led over the catalyst at a total flow rate of 50 mL min^{-1} (STP), equivalent to a weight hourly space velocity (WHSV) of 60,000 mL g^{-1} h^{-1}. The CO and CO_2 effluent gases were monitored via an IR analyser (ABB Uras 14).

3. Results and discussion

3.1. Synthesis and characterization of oxides

The different materials were prepared under similar synthesis conditions (microemulsion composition, pH, reaction time). Although certain turbidity appeared during the synthesis, the reaction mixture which remained after centrifugation and isolation of the particles was a single transparent phase, indicating that turbidity was due to the formation and certain agglomeration of nanoparticles. Hence, the microemulsion was stable during the synthesis. HRTEM studies revealed that in terms of particle size and shape, the nanoparticles were similar for the four types of materials prepared. The average particle size was 3.4, 2.5, 2.1 and 2.6 nm for CeO_2, $Ce_{0.5}Zr_{0.5}O_2$, ZrO_2 and TiO_2 nanoparticles respectively (Fig. 1a–d); the particles were globular in shape. As observed in Fig. 1a, CeO_2 nanoparticles had a greater tendency towards agglomeration in the microemulsion compared to the other materials, which appeared well dispersed (Fig. 1b–d). Certain agglomeration was also observed for $Ce_{0.5}Zr_{0.5}O_2$, ZrO_2 and TiO_2; these agglomerates were also made-up of small nanoparticles. HRTEM revealed that CeO_2 nanoparticles presented better crystallinity than the other materials.

XRD of the as-prepared samples (without calcination, Fig. 2a) presented well-defined peaks indicative of fluorite-type cubic structure for both CeO_2 and $Ce_{0.5}Zr_{0.5}O_2$. The d spacing for CeO_2 (3.116, 1.919 and 1.63 Å) were almost identical to those for the most intense peaks (d = 3.138 Å (1 1 1); d = 1.911 Å (2 2 0); d = 1.626 Å (3 1 1)) of c-CeO_2 in JCPDS card No. 04-0593[13]. The peak positions for $Ce_{0.5}Zr_{0.5}O_2$ were shifted to higher 2θ values and hence d spacings became smaller (3.04, 1.86 and 1.599 Å) as compared to CeO_2. A careful inspection of Fig. 2a, b suggests a certain asymmetry of the peaks which could be related to some tetragonality in the cationic sublattice due to the presence of zirconia richer phase [14].

For ZrO_2 two very broad peaks were detected, the strongest peak centred around 30.5° and the second peak ranging from 2θ = 50–60°, whilst for TiO_2, very broad and weak peaks were detected; this is typical for predominantly amorphous materials, and it was not possible to associate a specific crystalline structure. Given that the degree of crystallinity obtained for CeO_2 and $Ce_{0.5}Zr_{0.5}O_2$ was not achieved for ZrO_2 and TiO_2 the synthesis conditions have yet to be optimised for the latter materials, and at the current state crystallization may be achieved upon calcination; however, for the sake of comparison only materials synthesized following similar reaction conditions are described in the present study.

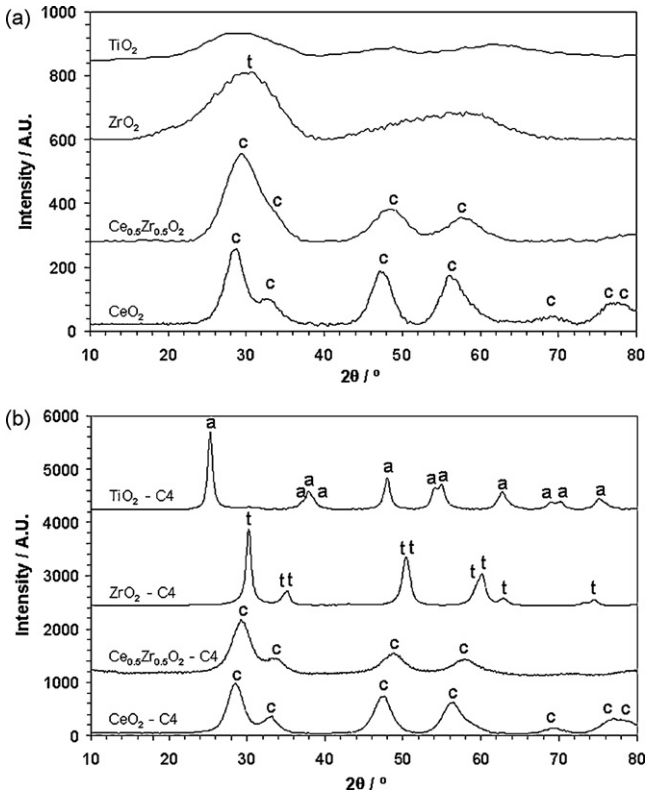

Fig. 2. XRD of CeO_2, $Ce_{0.5}Zr_{0.5}O_2$, ZrO_2, and TiO_2 nanoparticles obtained in o/w microemulsions: (a) as obtained (dried at 70 °C); (b) calcined (in air at 400 °C for 2 h). The positions for characteristic peaks of cubic CeO_2 and $Ce_{0.5}Zr_{0.5}O_2$ (c), tetragonal ZrO_2 (t) and anatase (a) phases are indicated.

Fig. 2b shows the XRD data for all the samples after being calcined during 2 h at 400 °C in air. The peaks for CeO_2–C4 and $Ce_{0.5}Zr_{0.5}O_2$–C4 corresponding to cubic type structure became more intense and better defined. For ZrO_2–C4 the crystallinity improved considerably after calcination, and all the peaks found were indicative of tetragonal phase. The crystallinity of TiO_2–C4 was also improved, and all the signature peaks for the anatase tetragonal phase could be identified; other phases (rutile and brookite) were absent. Concerning the presence of tetragonal phase of zirconia for particles of ca. 18.5 nm in the –C4 sample, the possible reason for the stabilization of the tetragonal phase rather than thermodynamically stable monoclinic one could be related to the relatively low particle size. In fact, it has been shown previously that a particle size ca. 30 nm is a turning point for phase transformation [15].

The approximate crystallite sizes as determined using the Debye–Scherrer equation are shown in Table 1, before and after calcination at 400 °C for all materials. ZrO_2 and TiO_2 presented

Table 1
Crystallite size (as calculated from Debye–Scherrer equation), specific surface area (SSA_{BET}), pore diameter (P_D), and pore volume (P_V) of CeO_2, $Ce_{0.5}Zr_{0.5}O_2$, ZrO_2, and TiO_2 nanoparticles obtained in o/w microemulsions, as obtained (uncalcined) and calcined at 400 °C.

Sample	Thermal treatment	Crystallite size/nm (XRD)	SSA_{BET}/m^2 g^{-1}	P_D/nm	P_V/cm^3 g^{-1}
CeO_2	as obtained	3.3	190.2	5.4	0.24
CeO_2–C4	calcined 2 h at 400 °C	4.5	159	5.1	0.19
$Ce_{0.5}Zr_{0.5}O_2$	as obtained	1.9	207	2.7	0.16
$Ce_{0.5}Zr_{0.5}O_2$–C4	calcined 2 h at 400 °C	3.7	107	3.2	0.07
ZrO_2	as obtained	1.1	377	3.0	0.27
ZrO_2–C4	calcined 2 h at 400 °C	18.5	116	3.1	0.09
TiO_2	as obtained	1.0	297	2.7	0.16
TiO_2–C4	calcined 2 h at 400 °C	16.1	124	4.7	0.20

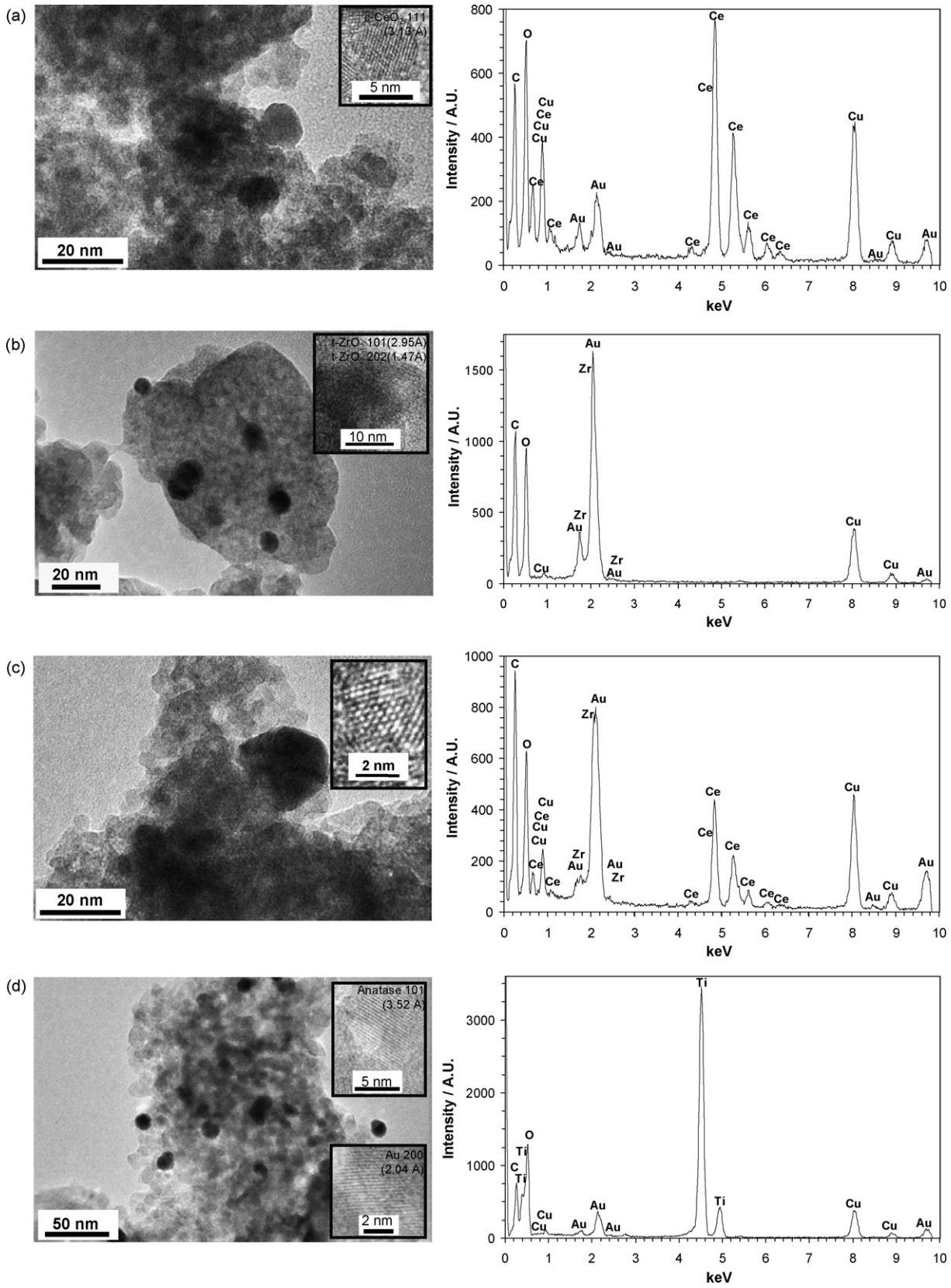

Fig. 3. HRTEM pictures (left) and EDX spectra (right) of (a) Au/CeO_2, (b) Au/ZrO_2, (c) $Au/Ce_{0.5}Zr_{0.5}O_2$, (d) Au/TiO_2. In the HRTEM pictures of (a) and (b), the inset shows high resolution (HR) of the support, whilst for (d) the top inset shows HR of the support and the bottom inset shows HR of Au; the values of the corresponding *d* spacings and Miller indexes are indicated. For (c), the corresponding *d* spacings are: 3.04 Å, 3.13 Å (c-CeO_2 1 1 1) and 2.95 Å (t-ZrO_2 1 0 1).

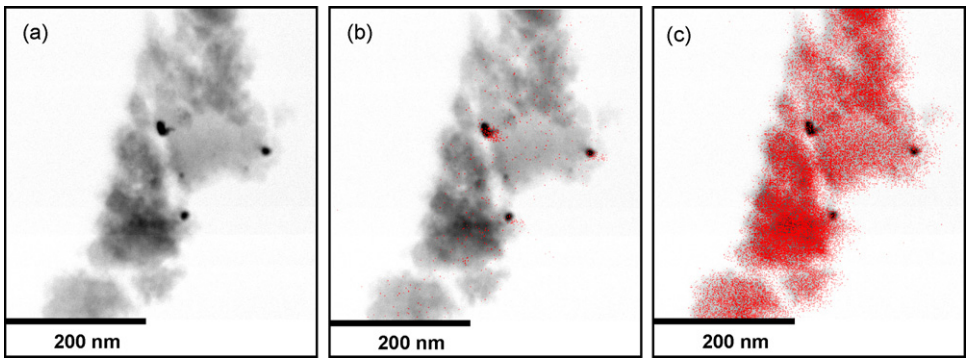

Fig. 4. Bright field TEM picture of the as-prepared Au/TiO_2 (a) showing the mapping of Au (b) and Ti (c).

the largest increase in crystallite size upon calcination, changing from ~1 nm for the as obtained materials to 18.5 and 16.1 nm after calcination for ZrO_2–C4 and TiO_2–C4 respectively. In contrast, the crystallite size of CeO_2 and $Ce_{0.5}Zr_{0.5}O_2$ increased only slightly after calcination.

BET areas and pore sizes are given in Table 1; rather high BET area values were obtained for all materials, with the highest value obtained for ZrO_2 (which presented also the smallest crystallite size by XRD). All the materials were mesoporous (pore size between 2.7 and 5.4 nm), and presented a narrow pore size distribution. After calcination at 400 °C, in general BET area and pore volume were reduced, whilst the pore size increased only slightly (maintained below 6 nm). However, each material responded differently to the calcination treatment, in terms of the magnitude of the change in properties. Whilst BET area of CeO_2 decreased only a 16.5% after calcination, for $Ce_{0.5}Zr_{0.5}O_2$, ZrO_2 and TiO_2 it decreased 48.3%, 69.3% and 58.4%, respectively.

In summary, the characterization results show that the different oxides, prepared using the same synthetic method in o/w microemulsions, follow the same trend in size, shape, surface area and porosity properties. The main difference is the different degree of crystallinity obtained, and as consequence the thermal stability towards sintering is also different. The material with better defined XRD peaks before calcination was CeO_2, and it was this material whose properties (specific surface area, crystallite size, porosity), changed less upon calcination. In contrast, the XRD of TiO_2 and ZrO_2 before calcination were less defined, but upon calcination the material became highly crystalline with very well-defined peaks and larger crystallite size, compared to CeO_2 and $Ce_{0.5}Zr_{0.5}O_2$. This crystal growth resulted in the largest change in specific surface area.

The $Ce_{0.5}Zr_{0.5}O_2$–C4 sample apparently lies somewhat out of such correlation and this is likely related to the presence of some zirconia segregation, according to the observed asymmetry of the XRD peaks (Fig. 2). Indeed, after calcination at 400 °C, the BET surface area of $Ce_{0.5}Zr_{0.5}O_2$ decreased a 48.3%, even if small crystallites size (3.7 nm) was maintained.

The pore size remain similar for all materials even after calcination, and this property is probably related with the characteristics of the microemulsion used as confined reaction media, which had the same composition in all cases except for the nature of the precursor. The differences observed must be related with the inherently different nature of the oxides, for which optimal preparation conditions should be investigated in order to favour the formation of nanocrystalline materials as achieved for CeO_2 and $Ce_{0.5}Zr_{0.5}O_2$.

3.2. Catalysts characterization

High resolution TEM with EDX was carried out for all the catalysts. Representative images and EDX analysis are shown in Fig. 3 for Au/CeO_2, Au/ZrO_2, $Au/Ce_{0.5}Zr_{0.5}O_2$ and Au/TiO_2 catalysts (Fig. 3a–d, respectively). On one hand, the characteristic particle size of the support material for the different samples as observed by TEM is in agreement with the crystallite size found for the calcined materials by XRD (by TEM: small, around 3–5 nm support particles for Au/CeO_2 and $Au/Ce_{0.5}Zr_{0.5}O_2$, whilst larger, around 10–20 nm support particles for Au/TiO_2 and Au/ZrO_2). The characteristic *d* spacings found for all the support materials were also consistent with their corresponding crystalline structures assigned by XRD analysis (see HRTEM insets in Fig. 3a–d, indicating their corresponding Miller indexes). In terms of the crystalline vs amorphous phases, from HRTEM it was confirmed that the support materials in Au/CeO_2, $Au/Ce_{0.5}Zr_{0.5}O_2$ and Au/TiO_2 were, at least at a qualitative level, mainly crystalline, whilst for Au/ZrO_2 crystalline zones were less common than amorphous zones. For the mixed oxide catalyst $Au/Ce_{0.5}Zr_{0.5}O_2$, careful HRTEM analysis shows that the main *d* spacings observed are in agreement with those found by XRD (mainly $d = 3.04$ Å) and to cubic CeO_2 (mainly $d = 3.138$ Å for 1 1 1 *hkl*), whilst *d* spacings for tetragonal ZrO_2 ($d = 2.95$ Å for 1 0 1 *hkl*) were only found in few zones.

With respect to the detection of Au, no gold particles of XRD detectable size are obtained in the as-prepared and used Au catalysts. However, by HRTEM/EDX technique, Au nanoparticles in the order of 10–20 nm where found, as observed in Fig. 3 for all the catalysts (observed as darker, spherical particles, and Au detected by EDX). Furthermore, it was possible to find the *d* spacings for crystalline Au for all the catalysts, and example high resolution image is shown in the inset to Fig. 3d ($d = 2.04$ Å for *hkl* 2 0 0). However, darker grey, blurry zones where a weak Au signal was detected by EDX may suggest possible smaller Au nanoparticles dispersed onto the supports. For deeper investigation, an EDX mapping of the elements was carried out for Au/TiO_2 catalyst. Fig. 4a shows the corresponding bright field image whilst Fig. 4b and c shows the maps where of Au and Ti were detected, respectively. Although the detection of Au mainly corresponds with the particles (or aggregates) of ~10–20 nm, weak Au signal was detected all along the aggregate, suggesting as well that Au is dispersed all along the support. The possible explanation for the generally weak Au signal is its low concentration (2 wt% with respect to the support in all cases). The used Au/TiO_2 catalyst was also characterized by HRTEM/EDX, as shown in Fig. 5. It presented similar characteristics to the as-prepared catalyst, in terms of support particle size, crystallinity and gold nanoparticle dispersion.

The XPS results are summarised in Table 3 in terms of the Au $4f_{7/2}$ binding energy and of the support element main peak energies. The Zr $2p_{3/2}$ and the Ti $2p_{3/2}$ are typical of ZrO_2 and TiO_2 respectively [16]. The experimental Au 4f photoelectron spectra of the four samples along with the corresponding curve fitting are shown in Fig. 6. In the case of $Au/Ce_{0.5}Zr_{0.5}O_2$ the curve fitting yielded one component characterised by $Au4f_{7/2}$ at 85.5 eV typical of ionic gold Au^{+1} [17]. In the case of Au/TiO_2 and Au/CeO_2 the

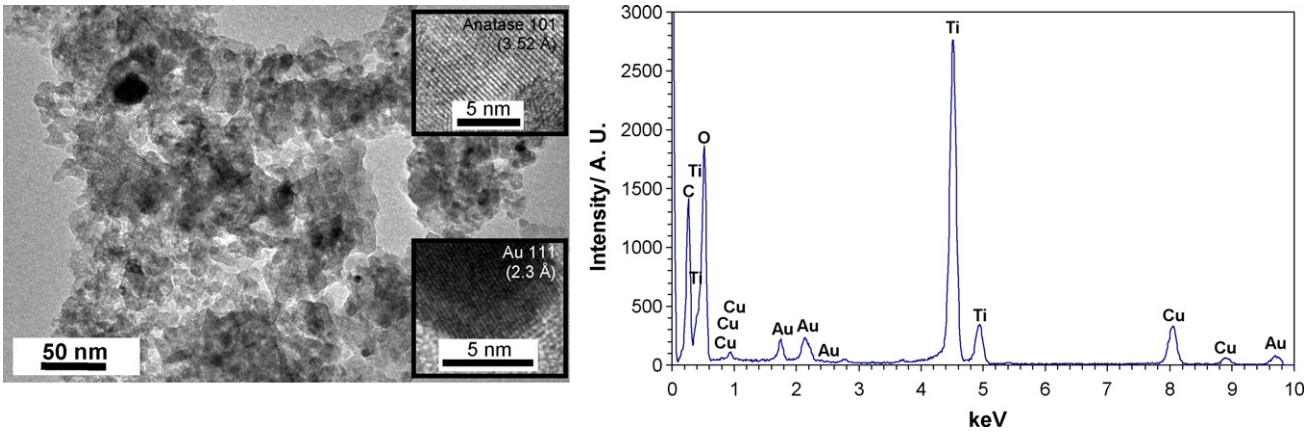

Fig. 5. HRTEM pictures (left) and EDX spectra (right) of used Au/TiO_2. In the HRTEM pictures two insets are shown corresponding to HR of TiO_2 at the top and Au at the bottom.

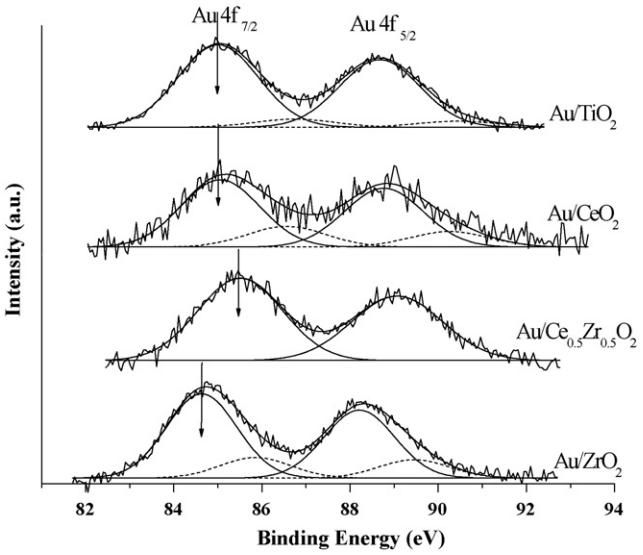

Fig. 6. Experimental and fitted Au 4f photoelectron spectra of the different catalysts.

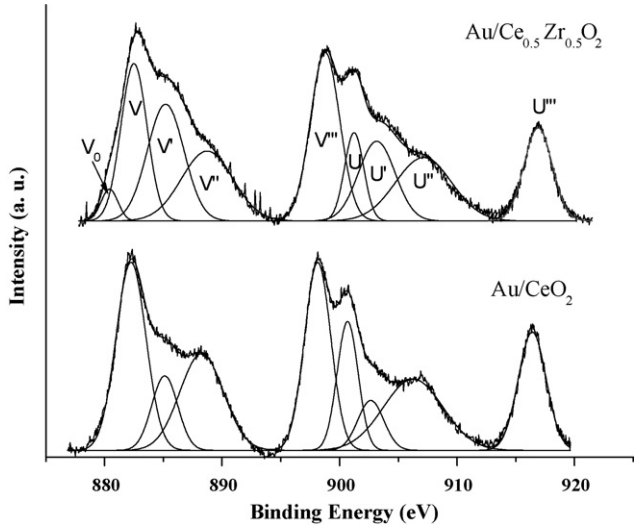

Fig. 7. Experimental and fitted Ce 3d spectra of two Au catalysts.

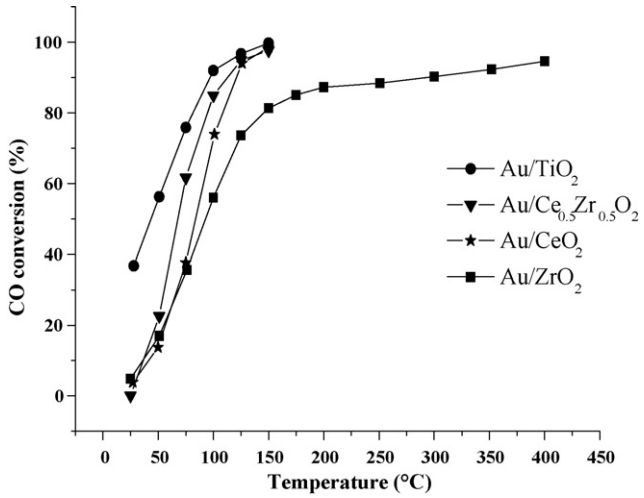

Fig. 8. CO conversion (%) as a function of temperature for Au supported catalysts.

curve fitting produced two components characterised, one by Au $4f_{7/2}$ at 85.0 eV still ascribable to Au^{+1} species and the other one at 86.6 eV typical of Au^{3+} [17]. The sample Au/ZrO_2 contains also two Au components, the most intense characterised by Au $4f_{7/2}$ at 84.6 eV typical of metallic gold and the other one at 85.8 eV typical of Au^{+1}. In Table 3 the relative ratios of the two components are given in parentheses. The surface atomic ratios between Au and the support elements are listed in the Table 3 along with the analytical (nominal) values in parentheses. In Fig. 7 the Ce 3d spectra of Au/CeO_2 and $Au/Ce_{0.5}Zr_{0.5}O_2$ are shown. The curves were fitted by several components corresponding to various pairs of spin-orbit doublets. The labelling of the peaks follows the convention adopted by Burrough et al. [18]. Letters U and V refer to the $3d_{5/2}$ and $3d_{3/2}$ spin-orbit splitting components respectively. Three pairs of peaks (V,U; V″,U″; V‴,U‴) arise from different Ce 4f electron configuration in the final states of the Ce^{4+} species [19]. The couple (V′,U′) corresponds to one of the two possible electron configuration of the final state of the Ce^{3+} species. In the case of the $Au/Ce_{0.5}Zr_{0.5}O_2$ catalyst

Table 2
Temperature (°C) at 50% CO conversion.

Catalyst	T_{50} (°C)
Au/TiO_2	44
$Au/Ce_{0.5}Zr_{0.5}O_2$	68
Au/CeO_2	84
Au/ZrO_2	93

Table 3
XPS binding energies of Au and main support peaks and atomic ratio of Au over support elements. The atomic percentages of each species are given in parentheses.

Samples	Au 4f 7/2	Ce 3d5/2	Zr 2p3/2	Ti 2p3/2	Au/Me[a]
Au/CeO_2	85.0 (76%) 86.6 (24%)	882.2 (88%) 885.1 (12%)			0.02 (0.018)
$Au/Ce_{0.5}Zr_{0.5}O_2$	85.5 (100%)	882.5 (68%) 885.2 (32%)	182.7		0.02 (0.015)
Au/TiO_2	85.0 (90%) 86.7 (10%)			459.2	0.016 (0.008)
Au/ZrO_2	84.6 (80%) 85.8 (20%)		182.8		0.016 (0.013)

[a] Me = Ce, Zr, Ti, (Ce+Zr); in parentheses the analytical ratios are given.

it was also possible to fit the V_0 state of the other Ce^{3+} final state configuration. The relative percentage of the two cerium species was estimated by the intensity of the Ce $3d_{5/2}$ components relative to Ce^{4+} (V,V′,V‴) and to Ce^{3+} (V′ and V_0). It is worth noticing the large amount of Ce^{3+} present in the mixed oxide supported gold.

For $Au/Ce_{0.5}Zr_{0.5}O_2$ catalyst, the atomic ratio between Ce and Zr was 1.3 which means a little more enriched in cerium as compared to the analytical one. With respect to other species such as chlorine carbonate and hydroxyl no differences between the Au/CeO_2 and the $Au/Ce_{0.5}Zr_{0.5}O_2$ samples are visible. No chlorine at all is detected.

3.3. Activity for CO oxidation

In Fig. 8 the CO conversion curves as a function of temperature are displayed for Au supported catalysts. In Table 2, the temperatures at 50% CO conversion (T_{50}) are listed. Au/TiO_2, $Au/Ce_{0.5}Zr_{0.5}O_2$ and Au/CeO_2 catalysts perform quite well, giving full CO oxidation within 150 °C. At low temperature, Au/TiO_2 is the most active, with T_{50} of 44 °C, followed by $Au/Ce_{0.5}Zr_{0.5}O_2$ and Au/CeO_2 giving 50% of conversion at 68 and at 84 °C, respectively. Au/ZrO_2 shows the lowest activity, converting 50% of CO at 93 °C; moreover it does not reach complete CO conversion in the range of temperature explored (up to 400 °C), the maximum conversion of CO achieved was 95%.

The surface atomic ratios between Au and the support, which were determined by XPS (Table 3), show a high dispersion of gold on TiO_2 with respect to the nominal values. The higher dispersion is responsible for a higher number of surface catalytic sites. These findings are in agreement with the catalytic behaviour, since Au/TiO_2 is the better performing catalysts in CO conversion at low temperature.

A Langmuir–Hinshelwood mechanism is proposed for Au/TiO_2, suggesting oxygen molecules adsorption at the particles edge and the O–O bond being stretched by electron transfer from Au, which is initiated by the presence of Ti cations and oxygen vacancies at the interface [20]. The Au/oxide interface is, therefore, regarded as the active phase. As a result, the high dispersion of Au on TiO_2 leads to higher Au nanoparticles surface area and enhanced catalytic activity.

It is also worth noting the superior performance of $Au/Ce_{0.5}Zr_{0.5}O_2$ with respect to Au over the pure oxides. The XPS analysis reveals an increase of oxygen vacancies in the mixed oxides, since a higher percentage of Ce^{3+} is present compared to pure CeO_2.

For Au/CeO_2, a mechanism involving the support is proposed. Indeed, due to the oxygen storage capacity, the easy reducibility and the high mobility of surface lattice oxide ions, ceria can act as an oxygen supplier with a Mars-van Krevelen mechanism [21]. Therefore, an increase of oxygen vacancies in the mixed oxide could be responsible of the enhanced catalytic performances.

4. Conclusions

A novel oil-in-water microemulsion reaction approach for the synthesis of mesoporous nanocrystalline oxides with high specific surface area and uniform particle size has been developed. Upon calcination at 400 °C, the materials retain a high surface area, small crystallite size and mesoporosity. All the oxides prepared by this novel method were suitable support material for gold nanoparticles. The resulting catalysts show high support crystallinity and Au dispersion as observed by HRTEM/EDX and XRD. The obtained Au catalysts have shown activity in CO oxidation at low temperature. The highest activity was obtained with 2% Au/TiO_2 and 2% $Au/Ce_{0.5}Zr_{0.5}O_2$ with T_{50} of 44 °C and T_{50} of 68 °C respectively. The high activity of the 2% Au/TiO_2 was explained by an enhanced dispersion of the Au particles on the TiO_2 support. For the 2% $Au/Ce_{0.5}Zr_{0.5}O_2$, an increase of oxygen vacancies in the mixed oxides could explain its superior activity compared to the pure oxides.

Acknowledgments

This research work has been performed in the framework of the D36/003/06 and D43/004/06 COST Programme actions. M. Sanchez-Dominguez is grateful to CSIC for a JAE-Doc contract. Financial support from Ministerio de Ciencia e Innovación (MICIN, Spain, grant number CTQ2008-01979) and Generalitat de Catalunya (grant number 2009-SGR-00961) are aknowledged.

References

[1] B. Lindman, S.E. Friberg, Microemulsions: a historical overview, in: P. Kumar, K.L. Mittal (Eds.), Handbook of Microemulsion Science and Technology, Marcel Dekker, New York, 1999, p. 1.
[2] M.A. López-Quintela, C. Tojo, M.C. Blanco, L. Garcia Rio, J.R. Leis, Curr. Opin. Colloid Interface Sci. 9 (2004) 264.
[3] J. Eastoe, M.J. Hollamby, L.K. Hudson, Adv. Colloid Interface Sci. 5 (2006) 128.
[4] C. Destrée, J.B. Nagy, Adv. Colloid Interface Sci. 123–126 (2006) 353.
[5] M. Boutonnet, J. Kizling, P. Stenius, Colloids Surf. 5 (1982) 209.
[6] M. Boutonnet, S. Lödberg, E.E. Svensson, Curr. Opin. Colloid Interface Sci. 13 (2008) 270.
[7] M. Sanchez-Dominguez, M. Boutonnet, C. Solans, J. Nanopart. Res. 11 (2009) 1823.
[8] G.C. Bond, C. Louis, D.T. Thompson, Catalysis by Gold, I.C. Press, London, 2006.
[9] R. Zanella, S. Giorgio, C.H. Shin, C.R. Henry, C. Louis, J. Catal. 222 (2004) 357.
[10] M. Lamallem, H. El Ayadi, C. Gennequin, R. Cousin, S. Siffert, F. Aissi, A. Aboukais, Catal. Today 137 (2008) 367.
[11] D.A. Shirley, Phys. Rev. B 5 (1972) 4709.
[12] P.M.A. Sherwood, in: D. Briggs, M.P. Seah (Eds.), Practical Surface Analysis, Wiley, New York, 1990, p. 181.
[13] International Center for Diffraction Data, 12 Campus Boulevard, Newton Square, PA, USA, 1998.
[14] L.F. Liotta, A. Macaluso, A. Longo, G. Pantaleo, A. Martorana, G. Deganello, Appl. Catal. A 240 (2003) 295.
[15] M. Fernandez-García, A. Martinez-Arias, J.C. Hanson, J.A. Rodriguez, Chem. Rev. 104 (2004) 4063.
[16] J.F. Moulder, W.F. Stickle, P.E. Sobol, K.D. Bomben, in: J. Chastain, R.C. King Jr. (Eds.), Handbook of X-ray Photoelectron Spectroscopy, Phys. Electronics Inc., Eden Prairie, USA, 1995.

[17] M.P. Casaletto, A. Longo, A. Martorana, A. Prestianni, A.M. Venezia, Surf. Interface Anal. 38 (2006) 215.
[18] P. Burrough, A. Hamnett, A.F. Orchard, G. Thornton, J. Chem. Soc. Dalton Trans. 17 (1976) 1686.
[19] A. Kotani, T. Jo, J.C. Parlebas, Adv. Phys. 37 (1988) 37.
[20] L.M. Molina, M.D. Rasmussen, B. Hammer, J. Chem. Phys. 120 (2004) 7673.
[21] A.C. Gluhoi, H.S. Vreeburg, J.W. Bakker, B.E. Nieuwenhuys, Appl. Catal. A: Gen. 291 (2005) 145.